Desalination and Water Treatment
www.deswater.com

doi:10.5004/dwt.2017.20531

73 (2017) 30–45
April

Influence of dynamic operation of reverse osmosis systems on fluid dynamics and mass transfer by investigation of 2-D spacer filled channels

Alexander Präbst[a,*], Florian Kiefer[a], Alexander Kroiß[a], Markus Spinnler[a], Thomas Sattelmayer[a]

Lehrstuhl für Thermodynamik, Technischen Universität München, Germany, Tel. +49 89 289 16237, email: praebst@td.mw.tum.de (A. Präbst), kiefer@td.mw.tum.de (F. Kiefer), kroiss@td.mw.tum.de (A. Kroiß), spinnler@td.mw.tum.de (M. Spinnler), sattelmayer@td.mw.tum.de (T. Sattelmayer)

Received 29 July 2016; Accepted 19 January 2017

ABSTRACT

Motivation of this paper is the hypothesis of permeate flux enhancement due to the dynamic operation of Reverse Osmosis (RO) systems powered by fluctuating renewable energies or by active control. Therefore, in this paper the influence of laminar pulsating flows in spacer filled channels with two porous walls is considered and numerically analysed using the opensource Computational Fluid Dynamics (CFD) tool OpenFOAM. Three different 2-D spacer configurations typically found in literature are investigated: Cavity, Submerged and Zig-Zag. The simulations are performed using typical conditions for seawater desalination. A literature review about dynamically operated membrane systems showed that the results achieved in previous studies are contradictory. Most of them were experimentally or numerically performed in open channels at different conditions. A comparison of the results is therefore difficult. As a first approach this study discusses the dynamics of the mass transfer through the membrane using an analysis based on Biot number. For the CFD simulations, boundary conditions based on the Solution-Diffusion model are implemented and validated with literature data. It shows good agreement at steady state conditions for typical seawater and brackish water desalination conditions. A qualitative analysis of the flow patterns shows that the flow is mainly disturbed in the decelerating phase of the pulsation cycle, which increases the mixing inside the channel. Different local concentration profiles at the membrane and Sherwood number profiles showed that especially in the middle part of two cylinders the mass transfer is significantly influenced whereas at the attachment points of cylinder and membrane, the influence is only marginal. At Womersley numbers of Wo = 17.7 the concentration profiles along the membrane are highly disturbed and the patterns change significantly, also qualitatively. The influence of the Amplitude Ratio is lower than that of the influence of the Womersley number.

Keywords: CFD; Reverse osmosis; Pulsating flows; Spacer filled channels; Mass transfer enhancement

1. Introduction

Transport of mass and energy via fluid flow are unsteady in nature and technical applications. A comprehensive understanding of the dynamics in transient flows and their influence on heat and mass transfer would allow the exploitation of a larger spectrum of processes [7]. In spite of its high technical relevance, some of the observed effects of time-periodic flows and the impact on scalar transport are not sufficiently supported by theory. On this basis, researchers have studied the mass transfer enhancement due to dynamic operation of membrane systems. Nevertheless, it is controversially discussed if a dynamic operation mode has the ability to enhance the

*Corresponding author.

Presented at the EDS conference on Desalination for the Environment: Clean Water and Energy, Rome, Italy, 22–26 May 2016.

1944-3994 / 1944-3986 © 2017 Desalination Publications. All rights reserved.

permeate flux in a membrane system and this reduce its energy consumption.

Zamani et al. [1] studied the influences of different strategies to increase wall shear stress at the membrane and to enhance membrane processes. They reviewed particle fluidization, vibrations, gas sparging and pulsations for different membrane systems. Considering reverse osmosis (RO), the vibration technology has the highest impact on the enhancement but it needs the highest energy input [1]. For pulsating flows they did not find any data about energy consumption. Emad et al. [2], Reverberi [3] and Kennedy et al. [4] numerically studied pulsating velocities in pipe and open channel geometries and stated a performance increase in RO processes. Kennedy [4] validated a model, developed by Ilias and Govind [1,5] and indicated that at pulsations of 1 Hz, an increase over 70 % of permeate production could be reached in RO processes. Baikov et al. [6] also investigated the phenomenon of mass-transfer enhancement in pulsating RO processes analytically. They calculated an optimum frequency of around 3 Hz, which match their experiments.

Another studies found in literature also reveal that a pulsating in flow decreases the fouling potential. The appearance of periodic peaks of wall shear stress in a time-periodic internal flow may enhance the removal and prevention of deposits within piping systems used in the processing of biomaterials [7]. Generally, it is well known that oscillatory flows influence the dispersion of particles or contaminants [7,8,9].

Gupta et al. [10] performed an experimental study about ultrafiltration and microfiltration operated by a pulsating piston cylinder apparatus and observed a permeate output increase of around 45%, whereas the hydraulic power could be reduced up to 30%. Jaffrin et al. [11] observed a 30–60% increase in membrane Plasmapheresis and Bertram [12] demonstrated a 60% flux increase in microfiltration. Abbas et al. [13] noted in their studies about flux enhancement in RO processes that a salt passage could be decreased due to the high salt rejection of the membrane but at 1 Hz the permeate flux could be increased up to 10% for the maximum time variant permeate rate. Ali et al. [14] found a 42% increase and 20% salt passage reduction in a tubular RO membrane under pulsating flow conditions at 1 Hz. Al-Bastaki and Abbas [15] reached a permeate increase from 0.3–13% for different frequencies in tubular RO membrane modules. The dynamics of these fluctuations are comparable to the fluctuations of wind velocity or solar radiation (due to clouds) [16]. Some researchers also argued that these fluctuations enhance the permeation production of RO systems, if they are directly connected to the fluctuating power supply. Nevertheless Richards et al. [16–20], who investigated transient powered wind- and solar-RO systems, did not see any improvement of the performance due to such slow perturbations. They stated that there is a performance decrease compared to steady state operation. Thomas et al. [21] numerically studied the mass transfer in pulsatile flows in tubular RO membranes, but they did not observe a performance enhancement but even a decrease. Rodrigues et al. [22] experimentally studied frequencies of 10 Hz and 50 Hz at different Reynolds numbers in spacer filled channels and observed a permeate flux increase up to 50% at a pressure loss increase of only 10%. They denoted that the effect will decrease over the length of the membrane since the perturbations are much higher near the pulsation generator. The details of the beneficial effects are not explained in their paper.

In most of the studies, except of Rodrigues et al. [22], simple open-channels or pipes without turbulence promoters are considered. It can also be seen that the results of the different authors differ significantly from each other. One important point, which is to be mentioned here, is the generation of pulsating flows, amplitudes and frequencies. To guarantee specific oscillations inside the membrane channel is a very challenging task and it is difficult to reproduce it, which might explain the divergent experimental results in literature. Due to this fact it is difficult to determine different effects of mass transport enhancement.

To give an idea about possible hydrodynamic and thermodynamic phenomena occurring in spacer-filled channels under a laminar pulsating flow regime without any side effects given in experiments, a systematic study of mass transfer enhancement should be done in a representative geometry. It is the aim of this paper to give an idea about which parameters induce a significant mass transfer enhancement in a simplified but representative geometry of Spiral Wound Modules (Cavity, Submerged and Zig-Zag spacer configuration).

2. Mathematical problem and theoretical background

2.1. Governing equations

Mass conservation, Newton's second law and a convection-diffusion equation are solved using the Finite Volume Method. Here, only the strong formulation of the problem will be given. Having a fluid with density, $\rho = \rho\ (x,t)$ the continuity equation reads

$$\frac{\partial \rho}{\partial t} + \nabla \cdot (\rho \mathbf{u}) = 0 \cdot \tag{1}$$

The momentum equation is given in the conservative form:

$$\frac{\partial (\rho \mathbf{u})}{\partial t} + \nabla \cdot \left((\rho \mathbf{u}) \cdot \mathbf{u}^T \right) = \nabla \cdot \boldsymbol{\sigma} + \rho \mathbf{b}, \tag{2}$$

where σ denotes the Cauchy stress tensor and b the applied body force. σ is defined as follows:

$$\boldsymbol{\sigma} = -p\mathbf{I} - \frac{2}{3}\mu \left(\mathrm{tr}\left(\varepsilon(\mathbf{u}) \right) \right) + 2\mu\varepsilon(\mathbf{u}), \tag{3}$$

where ε is given as the strain rate tensor:

$$\varepsilon = \frac{1}{2}\left(\nabla \mathbf{u} + (\nabla \mathbf{u})^T \right) \cdot \tag{4}$$

The convection-diffusion equation of the mass fraction ϕ can be formulated as follows:

$$\frac{\partial (\rho\phi)}{\partial t} + \nabla \cdot \left(\mathbf{u}(\rho\phi) \right) = \nabla \cdot \left(\mathrm{D}\nabla(\rho\phi) \right) + \dot{S}_\phi, \tag{5}$$

where $D = D(\mathbf{x},t)$ is the diffusion coefficient for NaCl in water and $\dot{S}_\phi$ is a source term.

Here, no source of mass is needed, $\dot{S}_\phi = 0$. Excess enthalpies are neglected, therefore the process is iso-thermal. The temperature is kept constant at $T = 298.15$ K.

Every well-conditioned problem needs consistent initial as well as boundary conditions for all times. Therefore, the boundary $\partial\Omega\ \Gamma_D \cap \Gamma_N$ of the fluid domain is divided in a Dirichlet $\Gamma_D = \partial\Omega \backslash \Gamma_N$ and Neumann $\Gamma_N = \partial\Omega \backslash \Gamma_D$ part with prescribed Dirichlet boundary conditions (DBC) and Neumann boundary conditions (NBC). Time-dependent conditions at the boundaries are given as:

$$\mathbf{u}(\mathbf{x},t) = \mathbf{u}_D(\mathbf{x},t), \quad \forall \mathbf{x} \in \Gamma_D, \quad \forall t \tag{6}$$

$$\boldsymbol{\sigma}\left(\mathbf{u}(\mathbf{x},t), p(\mathbf{x},t)\right) \cdot \mathbf{n} = \mathbf{h}_N(\mathbf{x},t) \quad \forall \mathbf{x} \in \Gamma_N, \quad \forall t \cdot \tag{7}$$

The initial condition at time $t = t_0$ for the primary variable u is

$$\mathbf{u}(\mathbf{x},t_0) = \mathbf{u}_0, \quad \forall \mathbf{x} \in \Omega \cdot \tag{8}$$

2.2. Description of pulsating flows

Pulsating flows can be characterized by a composition of a mean and a time oscillating component. The terms for pulsating flows used in the literature are sometimes misleading. This work will use the definition adopted from [23]. A pulsating flow denotes a steady state component superimposed with a time oscillating component. An oscillating flow is therefore a sub-branch of pulsating flow with vanishing mean part. The periodic behaviour can be described by a superposition of three components

$$\mathbf{u}(\mathbf{x},t) = \mathbf{u}_0(x) + \tilde{\mathbf{u}}(\mathbf{x},t) + \mathbf{u}'(\mathbf{x},t), \tag{9}$$

where $\mathbf{u}_0(\mathbf{x})$ denotes the mean component, $\tilde{u}(x,t)$ describes the periodic oscillations with an angular frequency and a non-periodic or stochastic component $u'(x,t)$**.** This can be exemplarily seen in Fig. 1.

In spiral wound modules, the flow is stated as laminar for typical operation conditions [24]. In pulsating flows, the critical Reynolds number can be significantly decreased or increased, depending on frequency and amplitude [25]. According to [26] four flow regimes can be identified in pulsating flows [27]:

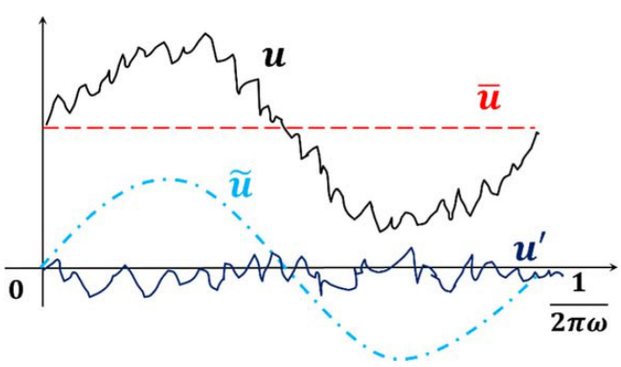

Fig. 1. Tri-Composition in a steady, periodic and stochastic fluctuating part of pulsating velocity, adapted from [23].

(1) laminar flow,
(2) disturbed laminar flow: small perturbations in the acceleration phase of the cycle,
(3) intermittently turbulent flow: turbulent transition at the beginning of the deceleration of the cycle, while laminar flow is dominant during acceleration,
(4) fully turbulent flow over one cycle.

In the present study the Reynolds number are below 200, thus it can be assumed that turbulence can be neglected. Nevertheless, the results, discussed later on, show that there is a difference between the acceleration and deceleration phase. It is assumed, that the flow could be classified into the above described schemes between phases two and three. A more detailed study is on beyond the scope of this paper.

2.3. Physical parameters

For the presentation of the results, different dimensionless numbers are introduced to get a more general picture of the problem. In pulsating flows, the amplitude ratio AR and the Womersley number Wo are characteristic values. Wo is the ratio between the dynamic viscous and convective forces and AR compares the unsteady velocity to the mean velocity:

$$AR = \frac{max\left(\left\|\tilde{\mathbf{u}}(\mathbf{x},\mathbf{t})\right\|\right)}{\left\|\mathbf{u}_0(\mathbf{x},t)\right\|}, \tag{10}$$

$$Wo = \sqrt{\frac{L^2\omega}{\upsilon}} = \sqrt{2\,\pi\, Re \cdot Str}, \tag{11}$$

where Re is the Reynolds number

$$Re = \frac{L\left\|\bar{\mathbf{u}}\right\|}{\nu} \tag{12}$$

and Str is the Strouhal number

$$Str = \frac{\omega L}{2\pi\left\|\bar{\mathbf{u}}\right\|} = \frac{f\,L}{\left\|u\right\|} \cdot \tag{13}$$

where f is the frequency, ω is the angular frequency, $\|\mathbf{u}\|$ velocity magnitude and L is the characteristic length of the considered problem. Here, the channel height was chosen to make it comparable to other studies and the channel geometry. The mass transfer will be described by the Sherwood number

$$Sh = \frac{\bar{\beta}\,L}{D} = \frac{(\mathbf{n}\nabla\phi)_{wall}\,\boldsymbol{L}}{\left(\phi(\mathbf{x})_{bulk} - \phi_{wall}\right)}, \tag{14}$$

with

$$\bar{\beta}\left(\phi(\mathbf{x})_{bulk} - \phi_{wall}\right) = D(\mathbf{n}\nabla\phi)_{wall}. \tag{15}$$

$\bar{\beta}$ is the time averaged mass transfer coefficient. The bulk mass fraction is calculated using the velocity and the mass fraction distribution:

$$\phi(\mathbf{x})_{bulk} = \frac{\int_0^H \|\mathbf{u}(\mathbf{x})\| \phi(\mathbf{x}) dy}{\int_0^H \|\mathbf{u}(\mathbf{x})\| dy}. \tag{16}$$

The Membrane Peclet number is defined as:

$$Pe_{mem} = \frac{L_0 u_{mem}}{A_{mem}}. \tag{17}$$

L_o is the thickness of the heat or mass transferring wall, u_{mem} is the velocity of the liquid through the membrane and D_{mem} is the diffusion coefficient inside the active layer of the membrane.

In transient mass transport phenomena the Biot number Bi is a measure for the dynamics between convective mass transfer and diffusion:

$$Bi = \frac{L_0 D_{mem}}{1/\beta}. \tag{18}$$

and D_{mem} is the diffusion coefficient of water or salt through the mass transfer wall. In spacer filled channels the concentration polarization factor Γ_{cp} is used to evaluate the mixing efficiency of the spacer:

$$\Gamma_{cp} = \frac{\phi_{mem}}{\phi_{bulk}}. \tag{19}$$

2.4. Identification of dynamics in the reverse osmosis process

The fully transient mass and momentum transport problem can be divided into different occurring dynamic phenomena. Due to the change in the mean flow velocity the local mass transfer coefficient $\beta(\mathbf{x},t)$ will change over time. There are also some dynamics in the membrane itself: solution and diffusion, whereas diffusion is the rate limiting step [28]. A graphical description of the dynamic "cascade" of the problem can be seen in Fig. 2.

Lighthill [29] studied the response of a hydrodynamic boundary layer to fluctuations of small amplitude in the external flow. He found out that a specific phase lag occurs between the bulk velocity and the mean velocity of the boundary layer. He further assumed that the boundary layer will perform small harmonic oscillations at a harmonic bulk-flow perturbation. At distances far away from the wall, the phase lag vanishes and the velocity amplitudes tends to the far field. Due to viscous forces in the boundary the velocity magnitude near the wall is smaller than in the bulk and therefore the inertia. This means that it can respond faster to external perturbations [23].

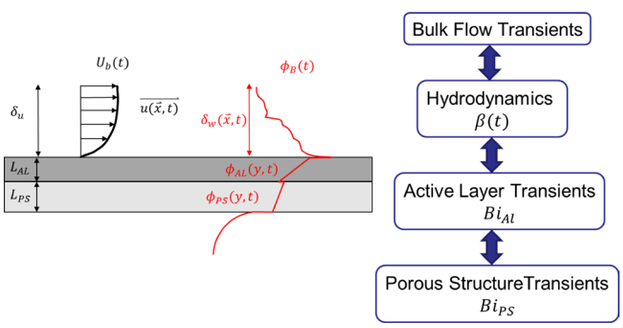

Fig. 2. Graphical description of pulsating flows in Reverse Osmosis processes including membrane dynamics (active layer; porous structure including support layer), adapted from [23].

At different frequencies and amplitude ratios different phenomena concerning the flow field can be identified in plate, open-channel and pipe flows without turbulence promoters. The first one is the so called Richardson effect [30]. The dynamics of the bulk affect the surface shear and generate a sinusoidal maximum in the velocity profile nearer to the wall. The next important phenomenon in pulsating flows is flow reversal, i.e. the coexistence of positive and negative flow velocities in a profile at an instant in time. It has been shown (see for example [7]) that this flow reversal begins near the wall for high pulsation frequencies, dependent on amplitude, mean velocity and geometry. Detailed investigations about this phenomenon can be found in [7]. It is stated in [23] that these phenomena and instabilities in the boundary layer seems to contribute to a better mixing and diffusional back transport and therefore to a higher heat or mass transport.

The dynamics in the boundary layer have an effect on the transport of solute through the membrane, which has an own dynamic time scale. Usually, in a typical operation, these dynamics can be totally neglected [31]. The dynamics of the pulsating flow are much higher compared to the usual operation modes, which can be in the range of the dynamics inside the active layer (AL) and porous structure (PS) layer. Using the Sherwood equations of Schock and Miquel [32] and approximated membrane diffusion coefficients from molecular dynamics simulations of Luo et al. [33], a mass transfer Biot number can be calculated:

$$\begin{aligned} Bi &= \frac{L_{AL,PS}/D_{AL,PS}}{1/\bar{\beta}} = Sh\frac{L_{AL,PS}D_{AB}}{d_h D_{AL,PS}} \\ &= 0.065\,Re^{0.875}Sc^{0.25}\frac{L_{AL,PS}D_{AB}}{d_h D_{AL,PS}}. \end{aligned} \tag{20}$$

The diffusion coefficients in the porous structure are calculated using the structure parameter taken from [39] and the estimated thickness of a typical RO membrane (150 µm) and the diffusion coefficient taken from Luo et al. [33].

$$D_{PS} = D_{AB}\frac{L_{PS}}{S} \tag{21}$$

As it is mentioned before, the Biot number is a measure for the dynamics of a heat or mass transferring process. It can be seen in Fig. 3, that the Biot numbers for the active layer are far below 1, which indicates that the diffusion resistance through the membrane is much smaller than the mass transfer resistance from the fluid to the membrane. The resistance inside the porous structure is higher, which means that there can be a considerable dynamic compared to the mass transfer β. The higher the Reynolds number, the higher is the mass transfer coefficient. Thus Biot number increases, which can be seen in Fig. 3. In the present study

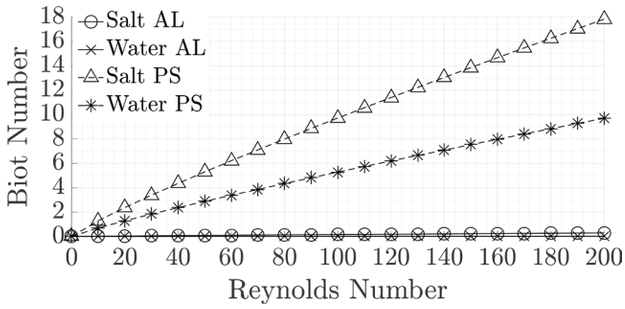

Fig. 3. Biot number of membrane active layer of 0.2 µm and support layer and porous structure of 150 µm thickness typically found in Spiral Wound Modules; the structure parameter is taken from [33] and represents a typical Thin Film Composite Reverse Osmosis membrane with S = 350 µm [33].

the focus lies on the phenomena inside the flow and transients inside the active and porous layers are neglected.

3. Methodology

3.1. Definition of a representative domain

According to Liang et al. [35], in Zig-Zag configuration, a developed hydrodynamic profile is reached after 5–6 cylinders depending on the Reynolds number. Therefore, for the geometry 10 cylinders are used. For the Cavity and Submerged type spacers, it was found that a steady velocity profile was developed after three filaments at the highest investigated Reynolds number of 200. The mass transfer is at the end of but still in the developing region for steady state conditions at Re = 200, which corresponds to the studies found in literature. The longest entrance length is given in the Submerged configuration. The ratio of distance between the filaments L and filament diameter D was chosen to be 4. The height of the channel is chosen to be 1 mm and the diameter 0.5 mm. Depending on the spacer and flow attack angle, the ratio can vary between 4 and 8 [35]. Another interesting point is that at an approximately distance of $L/D = 4$ between two cross-flow cylinders with a blockage ratio towards zero the flow patterns are classified as "jump region", a further increase would not change the flow patterns in theory [36]. A simplified scheme of the different domains can be seen in Fig. 4.

The inlet length was chosen $10 \cdot D$ before the spacer domain, to have a developed velocity profile before the first filament. To avoid backflow near the outlet after the last cylinder [37], the outlet was set $25 \cdot D$ behind the last cylinder. A mesh study shows that this outlet length was long enough to avoid vortices at the outlet boundary, which would lead to a diverging solution.

The mesh was generated using the Open FOAM tool snappy Hex Mesh. After a detailed mesh convergence study it was found that a detailed representation of the concentration and velocity-boundary layer can be realized with 20 prism layers placed on the membrane and 15 prism layers on the filaments. Due to the produced instabilities the gradients inside the layers are much higher than in steady state operation. The distance between the cell center of the first above the wall and the wall was set to 0.5 µm. The expansion ratio was set to 1.10, which results in a prism layer of around 50 µm.

The transient simulations were started from the steady-state at Re = 100 or Re = 200. Three Womersley numbers were chosen: 5.6, 7.9 and 17.7, which represent frequencies of 5 Hz, 10 Hz and 50 Hz. The Courant number was kept constant at 1. Due to the low mesh size and the Courant number the time step size was very small (< 1 µs) which results in a high computational effort. Higher Courant numbers would lead to numerical instabilities. The simulations were terminated when a quasi-steady-state is reached, which means in this study when the time averaged mass transfer over the membrane reached a residual of $1 \cdot 10^{-4}$.

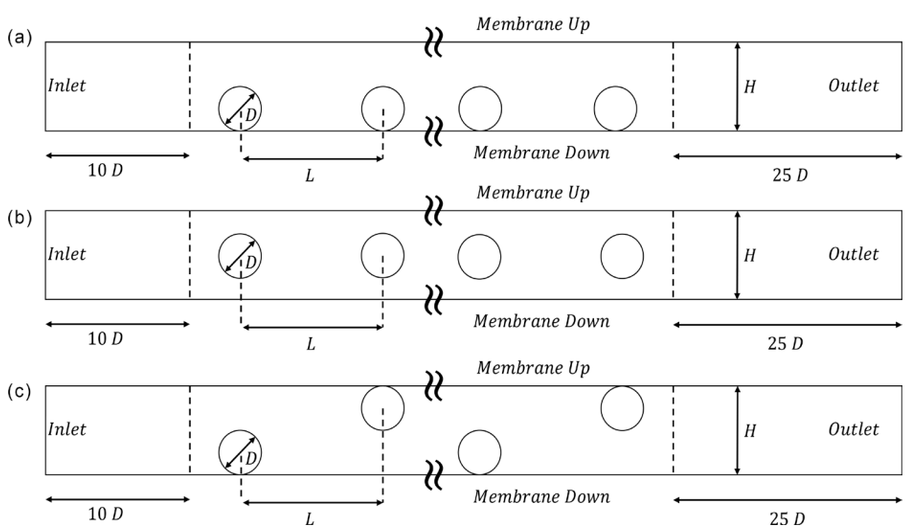

Fig. 4. Computational domains for the three different scenarios considered in this study; the diameter was chosen to , the channel height to 1 mm. (a) 2D Geometry for the Cavity type spacer configuration; (b) 2D Geometry for the Submerged type spacer configuration; (c) 2D Geometry for the zig-zag type spacer configuration.

One simulation of each configuration needs more than 20 days using 16 CPUs, a higher parallelization did not lead to lower computational time. The lower the frequency the higher is the time to reach a quasi-steady-state.

Due to the lack of experimental data for the present cases, a detailed mesh study was done to verify the results. The grid convergence index (GCI) [24] was calculated for every mesh at the highest occurring Reynolds number of 200. The GCI is based on a generalization of Richardson's extrapolation which goes back to Roach [38]. The GCI for fine and coarse grids can be calculated by

$$GCI_{fine} = F_s \frac{|e|}{1 - r^p} \tag{22}$$

and

$$GCI_{coarse} = F_s \frac{r^p |e|}{1 - r^p} \cdot \tag{23}$$

$|e|$ is the relative error for the calculations of the considered integral function, r is the refinement factor and p is the formal order of accuracy of the algorithm. F_s is a safety factor, which is here chosen as 1.25, which is adequately conservative [38]. Verification can be carried out if the GCi_ fine for the finest mesh falls below an acceptable error level below 1–5% [24]. For the calculation a *GCI* below 3% was taken, which was seen as converged. It can be seen from Fig. 5, that at a cell-number of around 280,000 to 300,000 the GCI for all values is below 3%. It is important to note that the GCI for different values (pressures, mass flux, mass fraction at the membrane) were investigated. The mass fraction needs the highest cell number to reach acceptable GCI values. Although the problem is not completely mesh independent, it is assumed that the error made is small. A good compromise is found between accuracy and simulation time, since the simulation of the transient problem needs a high computational effort.

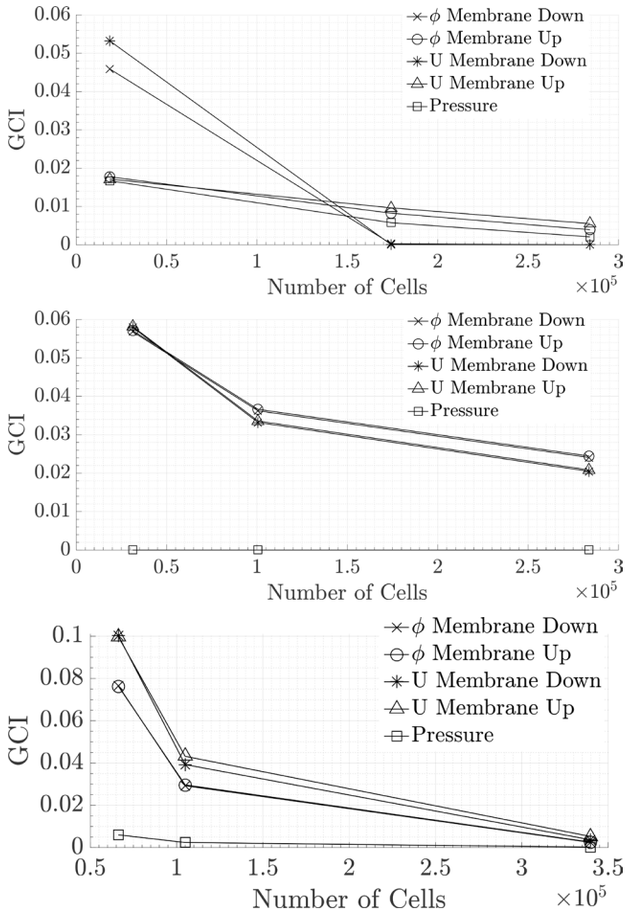

Fig. 5. Grid convergence study for different spacer configurations: Cavity, Submerged and Zig-Zag. (a) GCI_ study of the Cavity type spacer configuration; (b) GCI study of the Submerged type spacer configuration; (c) GCI study of the Zig-Zag type spacer configuration.

3.2 Numerical schemes and implementation into Open FOAM

As software platform Open FOAM 2.3.0 is used. To accurately represent the mass transport inside the computational domain [39], varying temperature and concentration dependent thermo-physical properties for the sodium chloride solution were implemented. As basis the equations of Sharqawi et al. [40] were used. The problem itself can be stated as an incompressible flow with variable thermophysical and transport properties at very low Mach numbers. Different studies in literature considering pulsating heat and mass transfer showed that these varying properties have a significant influence on the determined Nusselt or Sherwood number. For the solution of the Navier Stokes equations the full compressible solver rhoSimpleFoam for the steady state solution and rhoPimpleFoam for the transient simulation was modified. It was observed after some modifications of different solvers that the full-compressible approximation without resolving acoustic effects shows better convergence behaviour than a weakly-compressible approximation due to the stiffness of the solution matrix.

A study of different schemes was done to identify the most suitable ones. It was found out that second order schemes lead to the best results. For the time scheme Crank-Nicholson was used. For the divergence terms of the scalar transport equation the Van Leer Scheme leads to good results. The gradient terms were discretized using a linear central scheme. For the pressure and velocity gradients and divergence terms the limited linear scheme was used. Details about the different schemes can be found in [41].

The boundary conditions for the inlet, outlet and the walls were defined as can be seen in Table 1.

To accurately represent the diffusion through the membrane a boundary condition based on the solution-diffusion

Table 1
Boundary conditions for the considered computational domain

Boundary	Velocity	Pressure	Mass fraction
Spacer/walls	$u = 0$	$\nabla p = 0$	$\nabla \phi = 0$
Inlet	$u = u_0 (1 + AR (\sin(\omega t)))$	$\nabla p = 0$	ϕ = const.
Outlet	$\nabla u = 0$	p = const.	$\nabla \phi = 0$

model is implemented and iteratively solved. Due to the simplification using the salt rejection, which is often found in literature [24], especially at stagnation points at the membrane, non-physical behaviour was observed. The inaccurate local salt flux lead to the osmotic pressure differences between feed and permeate reaching values above the static pressure difference in the channel. The challenge to calculate the permeate quality was solved using a global salt mass balance.

$$\phi_{wall}\left(\dot{m}_{total}\right)+D_{AB}\nabla\left(\rho A\phi_{wall}\right)=\bar{\phi}_{perm}\dot{m}_{total} \tag{24}$$

$$\dot{m}_w=\rho_{w,wall}A_m A\left(\Delta p-\Delta\pi\right) \tag{25}$$

$$\dot{m}_s=B_m A\left(\rho_{s,wall}-\bar{\rho}_{s,perm}\right)\cong B_m A\rho_{wall}\left(\phi_{wall}-\bar{\phi}_{perm}\right) \tag{26}$$

$$\bar{\phi}_{perm}=\frac{1}{A}\int_0^B\int_0^L\frac{\dot{m}_s}{\dot{m}_w+\dot{m}_s}dxdz \tag{27}$$

$$\mathbf{u}_{wall}=\mathbf{n}\cdot\frac{\dot{m}_{total}}{\rho_w A} \tag{28}$$

Eqs. (24)–(28) are iteratively solved. The water permeability was chosen as A_m = 9.30·10^{-7} m^3 m^{-2} s^{-1} bar^{-1} and the Salt Permeability B_m = 7.96·10^{-7} m^3 m^{-2} s^{-1}, which were gained from experimental results in the institute's lab. The inlet mass fraction was set to ϕ_{Inlet} = 0.035 and a basic pressure of p_0 = 80 bar was set, which should represent useful operation conditions in seawater desalination systems. For simplification, concentration polarization is neglected at the permeate side. Since the permeate channel is infinitely long in the 2-D case, a complete and homogeneous mixing is assumed. These assumptions lead to a constant and global permeate concentration, which is dependent on the salt flux integrated over the membrane length. The error made by these assumptions is assumed to be relatively low, especially in a reverse osmosis system, where the concentration polarization on the permeate side is negligible. An error approximation using a modification of the flux-equation by Helfer et al. [34] was used to calculate the error:

$$\dot{V}_w=A_m\cdot\left(\Delta p-\frac{\pi_{F,b}exp\left(\frac{\dot{V}_w}{\beta}\right)-\pi_{p,b}exp\left(-\frac{\dot{V}_w S}{D_{AB}}\right)}{1+\frac{B_m}{\dot{V}_w}\left(\exp\left(\frac{\dot{V}_w S}{D_{AB}}\right)-exp\left(\frac{\dot{V}_w}{\beta}\right)\right)}\right) \tag{29}$$

Fig. 6 shows the approximated relative error with and without concentration polarization on the permeate side over the transmembrane pressure (TMP) for a feed mass fraction of $\phi_{feed,b}$ = 0.035 and a mean permeate mass fraction of $\phi_{perm,b}$ = 3.5·10^{-4}. The water permeability is set to A_m = 9.30·10^{-7} m^3 m^{-2} s^{-1} bar^{-1} and the Salt Permeability is varied to see the influence of the selectivity of the membrane. As the internal concentration polarization has more significant influence on this side of the asymmetric membrane [34], only this is considered. As it can be seen in Fig. 6 the error increases with lower salinity and decreases for higher transmembrane pressures (TMP). The error for *TMP* > 60 bar is below 4%, see Fig. 6 and decreases with higher transmembrane pressures. The higher the water flux, the lower is the salt concentration on the permeate side and the error decreases.

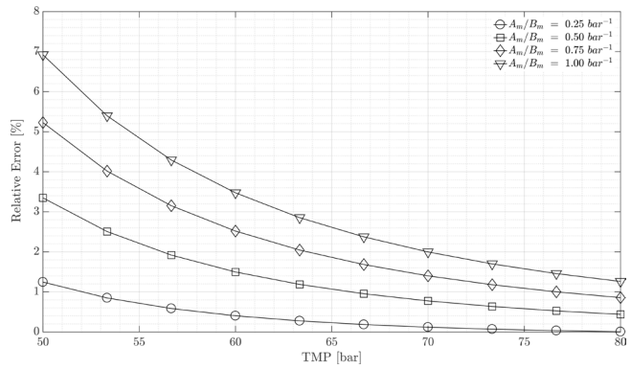

Fig. 6. Approximated relative error of neglecting concentration polarization on the permeate side for a RO membrane using Eq. (29) with varying ratios of A_m and B_m to represent high and low selective membranes; $\phi_{feed,b}$ = 0.035, $\phi_{perm,b}$ = 3.5·10^{-4} A_m = 9.30·10^{-7} m s^{-1} bar^{-1}.

4. Results and discussion

4.1. Validation of the boundary condition with literature data

To validate the solver and the implemented boundary conditions, data from Alexiadis et al. [42] for typical brackish water desalination conditions and Xie et al. [43] for typical seawater desalination conditions have been taken as reference. Alexiadis et al. [42] experimentally investigated an open-channel and compared a 2-D simulation with feed and permeate channels to the experiments. Contrary to Alexiadis et al. [42] only the feed channel is considered. The boundary conditions can be seen in Table 2.

For validation, the permeate flux was taken. It is assumed that the flux is a good indicator for validation of the boundary condition. If the mass transport and concentration polarization were not correctly reconstructed, the flux would differ depending on the occurring concentration polarization factor, which can range from 1.2 to 1.6, depending on the membrane Peclet number. This means that the permeate flux would also differ significantly. In Table A1 in the appendix, the results of simulation and experiment can be seen at different pressures and average feed velocities.

Table 2
Boundary conditions for validation study – data taken from Alexiadis [39]

Variable	Boundary condition	Unit
ϕ_{inlet}	0.002	–
Δp	8.89 … 13.98	bar
A_m	9.72·10^{-7} ± 0.3·10^{-7}	m bar^{-1} s^{-1}
u_{inlet}	0.15	m s^{-1}
T	298.15	K

The relative error ranges from 0.08 % up to 13.40 %, which is also summarized in Fig. 7.

From the experimental results it can be seen that the distribution of the flux is relatively high, even if the velocity, feed concentration and pressure stays almost the same. A specific error for each experiment was not given. The mean relative error between simulation and experiments is 4.8%. From Fig. 7 it can also be seen that the error between simulation and experimental results stays mainly below the mean error line and only few pass it.

For validation of typical seawater conditions experimental data from Xie et al. [43] were taken. Xie et al. [43] numerically (Comsol Multiphysics 4.2a) and experimentally investigated sinusoidal spacer configuration to enhance mixing in the boundary layer. They compared two spacer configurations and a straight channel with their experiments. The channels included sinusoidal patterns described by

$$y = a\sin\left(\frac{2\pi x}{b}\right), \tag{30}$$

where a is the amplitude and b is the wavelength. The cross-sectional geometry of the channel is 1.5 mm by 6 mm rectangle, with the membrane lying along on of the 6mm sides. The channels were 130 mm long in flow direction. The three investigated channel geometries can be seen in Fig. A1 in the appendix. It shows the top view of the channels. The flow direction is from left to right.

Five different cases were simulated for each channel. The inlet mass fraction ranges from 0.023 to 0.035 and the pressure from 55 to 69 bar. The boundary conditions can be seen in Table 3.

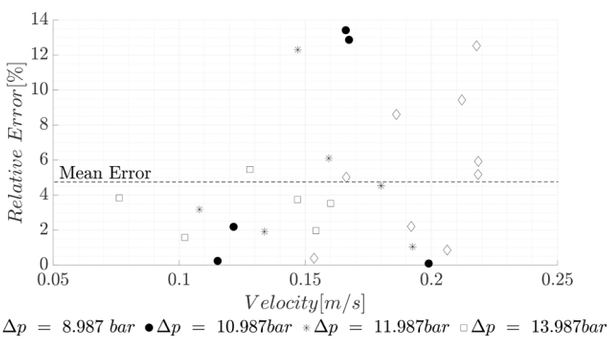

Fig. 7. Relative error of permeate flux between Open FOAM simulations and experimental results from Alexiadis et al. [41] – brackish water desalination conditions.

Table 3
Boundary conditions for validation study – data taken from Xie et al. [42]

Variable	Boundary condition	Unit
ϕ_{inlet}	0.023, 0.029, 0.035	
Δp	55, 62, 69	bar
A_m	$5.24 \cdot 10^{-7}$	m s^{-1} bar^{-1}
u_{inlet}	0.148	m s^{-1}
T	293.15	K

In Fig. 8 the simulation results are plotted against the experimental data. Similar to the simulation results of Xie et al. [43], there are some systematic variations, for example the simulations from the sinusoidal spacer under predict the experimental results. Nevertheless the modelling results are similar and it can be concluded that the CFD simulations are useful to predict the flux behaviour.

4.2. Qualitative flow analysis of pulsatile flows in spacer filled channels

In Figs. 9–11 different instantaneous velocity contours are shown at different times during a pulsation period, which can be seen on the right side of the figures. The black lines represent streamlines and the colours represent the relative velocity

$$\left\|\mathbf{u}_{rel}\right\| = \frac{\left\|\mathbf{u}\right\|}{\left\|\mathbf{u}_0\right\|}. \tag{31}$$

The flow pattern will be explained using the example of AR = 1 and Wo = 7.9.

In all three cases, at the beginning of the pulsation period t = 0, the flow patterns are similar to the steady state value and the typical flow encountered in 2-D channel flow can be seen.

In Fig. 9 the flow pattern inside the Cavity spacer during one pulsation period can be seen. During acceleration to Re = 200 the reattachment point moves downstream until the kinetic energy is high enough and there is no separation of flow. During deceleration it can be seen that there is still no reattachment although the Reynolds number was decreased to the initial value due to the fluid inertia. A further decrease to Re = 0 generates different vortex structures and disturbs the boundary layer. After acceleration to Re = 100 the flow reaches the initial status.

In Fig. 10 a pulsation period in the Submerged spacer can be seen. During acceleration, the recirculation bubble behind the cylinder upstream grows. In the decelerating phase the recirculation is disturbed and an a-periodic vortex separation occurs, which generates a higher mixing in the bulk flow. After deceleration to Re = 0, different vortices

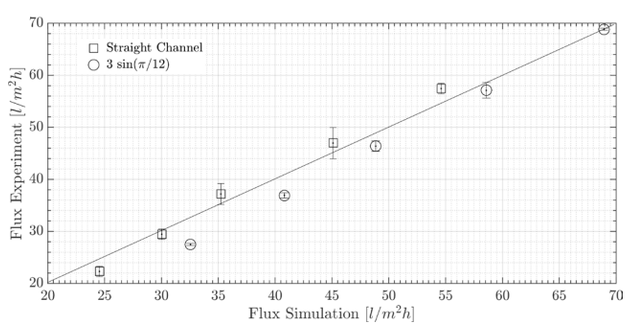

Fig. 8. Comparison of permeate flux between OpenFOAM simulations and experimental results from Xie et al. [42] – Seawater desalination conditions; the error bars show the standard deviation from experiments of Xie et al. [42].

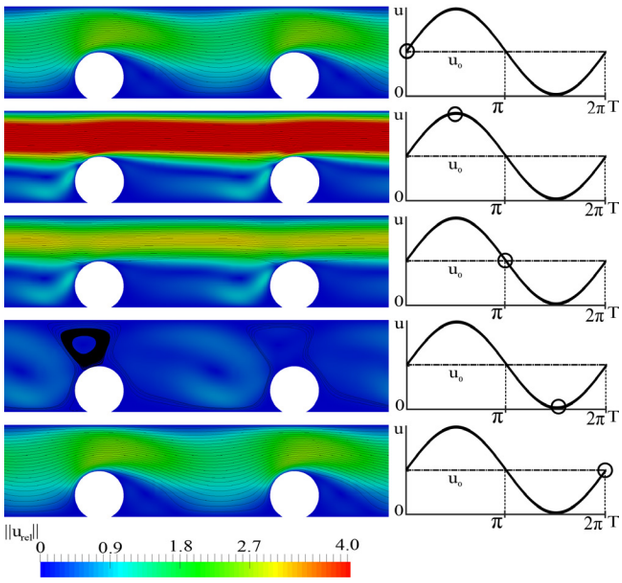

Fig. 9. Flow patterns and plot of the relative velocity of Cavity type spacer during one pulsation period; *AR* = 1, *Wo* = 7.9, *Re* = 100.

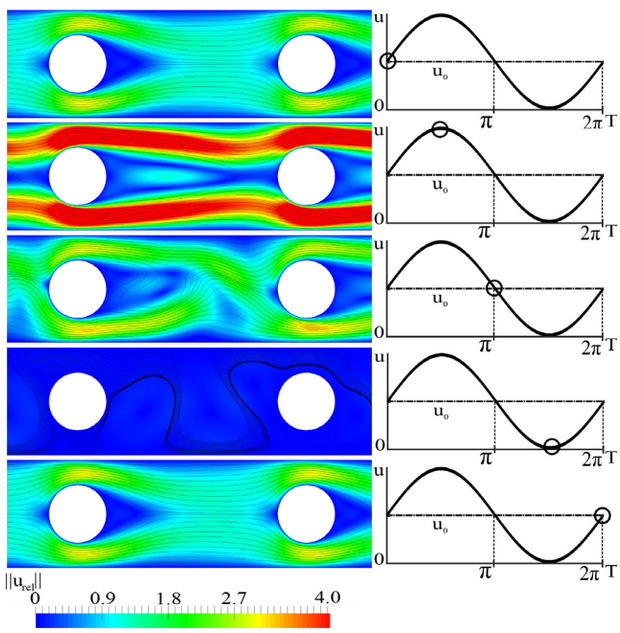

Fig. 10. Flow patterns and plot of the relative velocity of Submerged spacer during one pulsation period; *AR* = 1, *Wo* = 7.9, *Re* = 100.

over the height of the channel occur. After accelerating the process starts again.

In Fig. 11 the flow inside the Zig-Zag configuration is shown. At *Re* = 100 the reattachment point is almost in the middle of the two filaments. During the acceleration phase the reattachment point and the flow separation point at the upper cylinder move downstream. In the deceleration

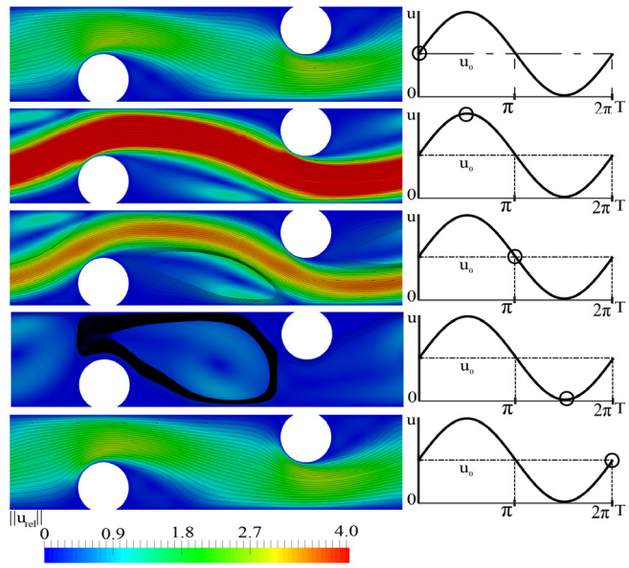

Fig. 11. Flow patterns and plot of the relative velocity of Zig-Zag spacer during one pulsation period; *AR* = 1, *Wo* = 7.9, *Re* = 100.

phase the separation zone "blows up" and the reattachment point stays almost at the same location.

It is obvious that the different phenomena occurring in pulsating flows in spacer-filled channels differ from that of the open channel (Richardson effect, flow reversal). The comparison of the studies found in literature considering open-channels will not give representative results about the mass transfer change in usual spiral wound modules due to a time-periodic inlet velocity. In the open-channel, the mass or heat transfer is significantly increased in the developing region of the boundary layer. It is assumed that due to the periodic perturbation of the attached cylinders, especially in the Zig-Zag configuration, the boundary layer has to develop periodically and is always in a kind of developing state. Therefore it is assumed that the spatial damping of the mass transfer enhancement along the flow direction, as reported in literature, differs a lot compared to the open channel.

4.3. Concentration polarization factor during a pulsation cycle

In this section the concentration field between two representative filaments during one pulsation cycle is considered, represented by the concentration polarization factor. It will be exemplarily discussed at *Wo* = 7.9 and *AR* = 1 and at quasi-steady state, which is reached for all configurations at least after 7 periods. The phenomena are explained between two spacer filaments ($x = 0 - L$, for Cavity and Submerged type; $x = 0 - 2L$ for Zig-Zag) in the hydrodynamically developed region. As it is explained in section 3.1 for Cavity and Submerged configuration, it is reached after 3 filaments and after 5 filaments for the Zig-Zag configuration. The upstream filament is at 0, the downstream filament is at $x = L$ or $x = 2L$. The considered section is in the middle of the computational domain to avoid influences from inlet and outlet boundaries. The results are presented in Fig. 11.

Due to the asymmetry in the Cavity type spacer the phenomena are discussed for the upper and lower membrane

separately. It can be seen from Fig. 12a that the concentration during one pulsation cycle is only marginally influenced. The highest change in concentration can be seen at $x = 0.75\ L$, which corresponds to the attachment point of the recirculation zone, see Fig. 9. Near the contact point ($x = 0, L$) between filament and membrane (0–0.125L;~0.875L–L) no influence can be seen. The phenomena at the upper membrane are completely different, see Fig. 11b. Considering the start of the pulsation period ($t = 0$), the influence of the flow expansion starting from $x = 0$ a momentum in normal orientation away from the membrane support the diffusional back transport and creates a minimum of concentration after the upstream cylinder. After expansion the velocity decreases and therefore the concentration increases.

The concentration polarization index curve in the Submerged configuration is qualitatively similar to the concentration profile of the upper membrane of the Cavity type spacer, see Fig. 11c. A slight change with a generation of a local minimum after the filament upstream during the deceleration phase can be seen. The maximum of the membrane concentration between two filaments stays almost at the same position. Especially in the developing region of the recirculation bubble the concentration is significantly influenced during acceleration (0π–π/2) and deceleration (π/2–π).

In the Zig-Zag configuration, compare Fig. 11(d), it can be seen that the pulsating bulk velocity influences the concentration change over time mainly in the middle of the two turbulence promoters at the bottom membrane during one pulsation cycle. Due to the changing of the recirculation zones between acceleration and deceleration (0π–π), which is in the Zig-Zag configuration near or directly below the upper filament, a momentum normal and therefore a convective transport of the bulk concentration to the membrane is generated at different locations during one cycle. During deceleration (π–3/2π) the mass transfer is decreasing due to the general low momentum. Near the attachment points of the spacer and the membrane, where the convective momentum is significantly lower, the concentration at the membrane is non-significantly changing.

In Table 4, the different mean values for the concentration polarization indices are given for the different configuration to compare the different geometries. The values given are in the hydrodynamically developed region. It can be seen that the highest concentration is given in the Cavity type configuration.

4.4. Effect of Womersley number on mass transfer

In this section, the effect of the Womersley number on the local mass transfer in each configuration is considered (Fig. 13). The results are again discussed between two filaments in the developed region during one pulsation cycle. The time averaged Sherwood numbers over one cycle at quasi-steady-

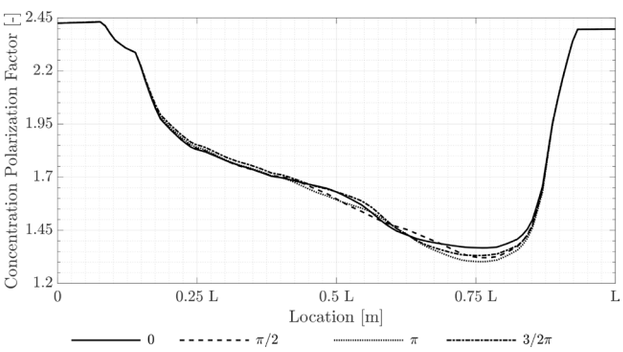

(a) Concentration polarization factor between two promoters at the membrane in the Cavity type configuration (down)

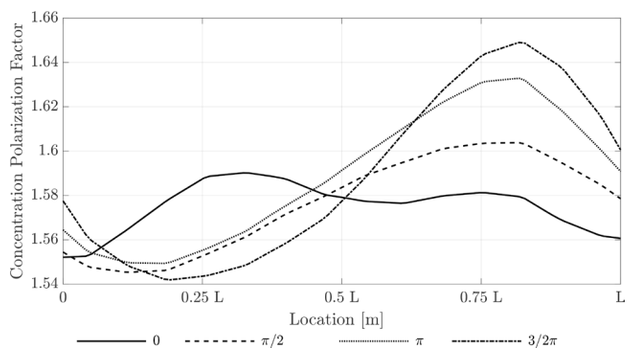

(b) Concentration polarization factor between two filaments at the membrane in the Cavity type configuration (up)

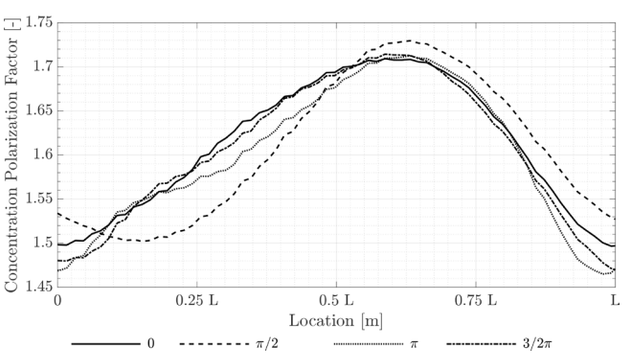

(c) Concentration polarization factor between two filaments at the membrane in the Submerged type configuration (down)

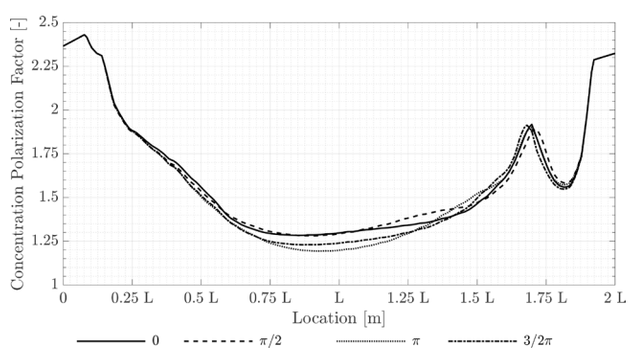

(d) Concentration polarization factor between two filaments at the membrane in the Zig-Zag type configuration (down)

Fig. 12. Concentration polarization factor between two filaments in the developed region for different geometries; a quarter of L corresponds to the diameter of the filaments: 0.25 L≙d; $AR = 1$, $Wo = 7.9$.

Table 4
Time integrated concentration polarization index values for the different 2-D spacer configurations after 3 or 5 filaments for the Cavity and Submerged or Zig-Zag configuration respectively

Spacer configuration	Womersley number	Amplitude ratio	Mean CP Index after 3 filaments
Cavity (down)	7.9	1.0	1.817
Cavity(up)	7.9	1.0	1.584
Submerged	7.9	1.0	1.532
Zig-Zag	7.9	1.0	1.576

state are taken to compare the enhancement of mass transfer. The amplitude ratio is kept constant at 1 which can be interpreted as a solenoid valve opening and closing in a specific frequency and sinusoidal way, which would be technically the easiest way to generate a pulsating inflow. The Womersley number is changed from *Wo* = 5.6 to 17.7.

In the Submerged configuration, see Fig. 12(b), the local Sherwood number profile can be seen as a "moved configuration" compared to the Zig-Zag configuration. Instead of a maximum, a minimum can be found in the middle between the two filaments at the lower membrane. This can be explained by the higher velocity at the locations of the cylinders due to the smaller cross section and is identical for steady-state and dynamic operation. At *Wo* = *17.7* the Sherwood number profile also changes qualitatively and the minimum moves upstream and crosses even the steady state line. At this frequency it is assumed that the high frequency strongly disturbs the flow behind the cylinder and the generated vortex separation increases the mixing inside the channel.

In the Zig-Zag configuration (Fig. 12(d)) it can be seen that the shape of the local Sherwood number does not change qualitatively between the two filaments for all considered Womersley numbers. It is interesting that the peak of the mass transfer is near the reattachment point of the location of the center of the upper cylinder, where the highest tangential velocity occurs. This indicates that a convective transport normal to the membrane is very important considering the improvement of the membrane process. This maximum stays at the same position even at different pulsatile operation modes. At *Wo* = 17.7 the maximum of the Sherwood number moves upstream. Under these conditions the local mass transfer is even increased almost totally over the length of one filament. The results also show that the local Sherwood number is the same for steady state and dynamic operation near the cylinders attachment points.

4.5. Effect of amplitude ratio

In this section the changing of the amplitude ratio at a specific Womersley number is investigated. The results are

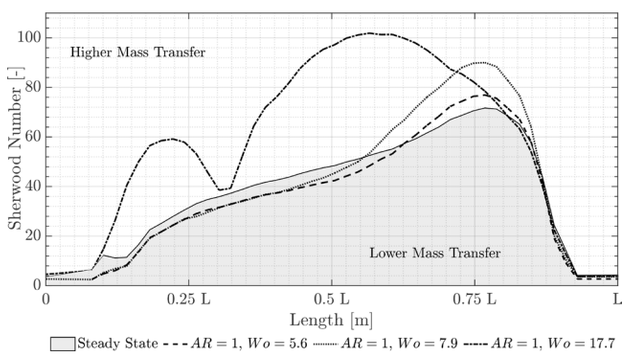

(a) Cavity-configuration: time averaged Sherwood number between two filaments at the membrane (down)

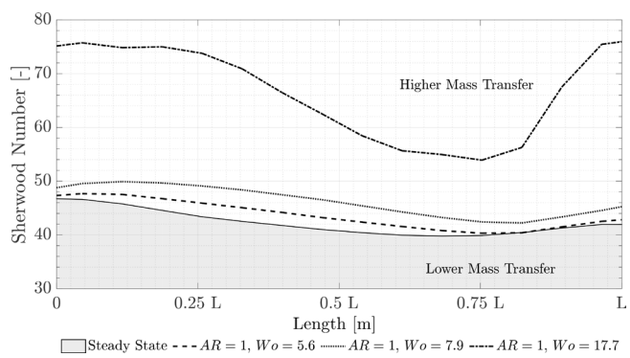

(b) Cavity-configuration: time averaged Sherwood number between two filaments at the membrane (up)

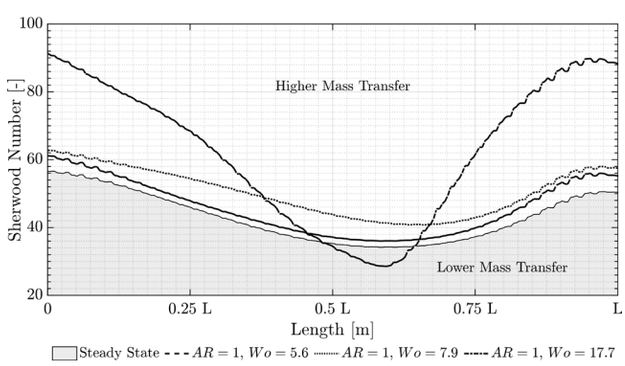

(c) Submerged-configuration: time averaged Sherwood number between two filaments at the membrane (down)

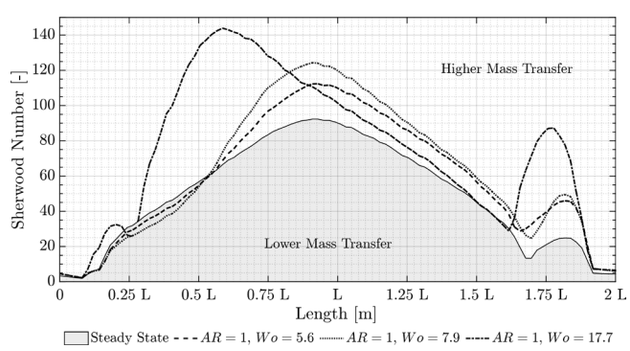

(d) Zig-Zag-configuration: time averaged Sherwood number between two filaments at the membrane (down)

Fig. 13. Time averaged Sherwood number over one cycle between two filaments in the developed region for different geometries; the grey area identifies the region of lower mass transfer compared to the steady state values; the results are presented for *AR* = 1, *Wo* = 5.6;7.9;17,7.

again discussed between two filaments in the developed region during one pulsation cycle and can be seen in Fig. 14. The AR is changed from 0.2 to 0.5 to 1. The Womersley number is kept constant at $Wo = 7.9$.

It is interesting that, contrary to the different Womersley numbers, in each of three geometries the Sherwood number profile along the membrane stays qualitatively the same for different AR. The maxima and minima of the mass transfer between the filaments stays at the same locations for the Zig-Zag and Cavity configuration. It also can be seen that the influence near the cylinder and membrane is only marginal. For the Submerged configuration the minimum is slightly moving downstream. Another interesting point for all three cases is the non-linearity in the enhancement over different amplitude ratios. The higher the pulsation amplitude the higher is the enhancement of the mass transfer and the influence at an amplitude ratio of $AR = 0.2$ is negligible or even lead to a decrease in mass transfer rate.

4.6. Mass transfer enhancement at different amplitude ratios and Womersley number

As discussed above, the enhancement of the mass transfer due to pulsating flow is a strong local and time dependent problem. To indicate and compare nevertheless the enhancement for the considered geometries and boundary conditions the mass transfer rate is integrated over length and time

$$\overline{\dot{m}}_{w,Puls} = \frac{1}{T}\int_{0+T}^{2\pi+T}\int_{0}^{L} \dot{m}_w dt dx \tag{32}$$

and plotted in Fig. 14 for different frequencies and amplitude ratios. The term enhanced mass transfer (EMT) is the ratio between mass transfer rate at pulsating conditions and mass transfer rate at steady state conditions.

$$EMT = \frac{\overline{\dot{m}}_{w,Puls}}{\overline{\dot{m}}_{w,stst}} \cdot \tag{33}$$

In Table A2 in the appendix the time and local averaged Sherwood numbers are given for the considered simulation.

It can be seen in Fig. 15 that with rising amplitude ratios, the mass transfer enhancement increases for all three considered configurations. It is also shown that the highest enhancement is at around 15–20 % for all three configurations. From $Wo = 7.9$ to $Wo = 17.7$ a non-linearity of over the changing AR can be seen. This can be explained by the disruption of the flow and the increased mixing. It can also be seen that at lower frequencies and amplitude ratios the pulsating mass transfer is even lower. In these cases the frequency is too low and the concentration boundary layer has the time for building up during the deceleration and acceleration (π–3/2π–2π) or the amplitude is too small to even disturb the boundary layer.

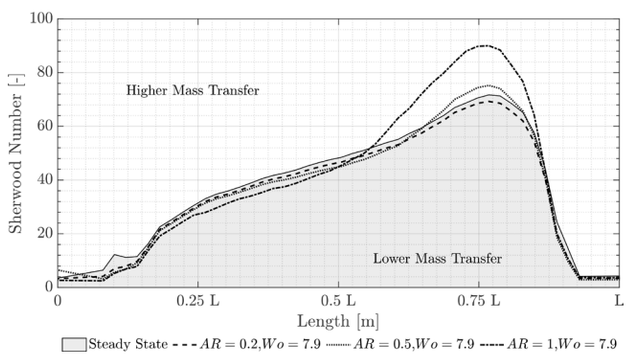

(a) Cavity-configuration: time averaged Sherwood number between two filaments at the membrane (down)

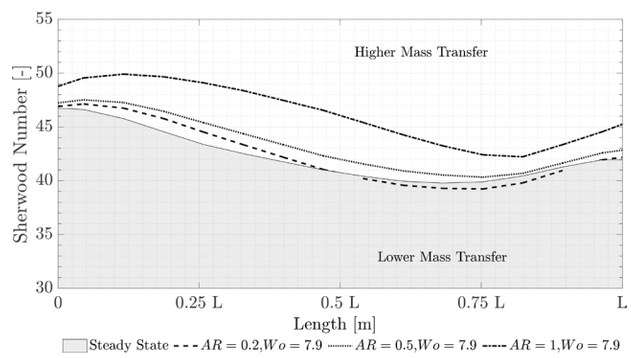

(b) Cavity-configuration: time averaged Sherwood number between two filaments at the membrane (up)

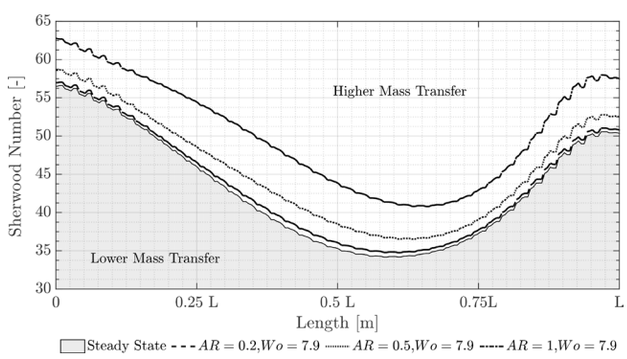

(c) Submerged-configuration: time averaged Sherwood number between two filaments at the membrane (down)

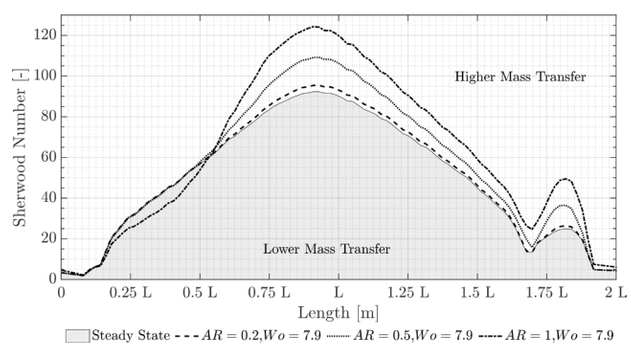

(d) Zig-Zag-configuration: time averaged Sherwood number between two filaments at the membrane (down)

Fig. 14. Time averaged Sherwood number over one cycle between two filaments in the developed region for different geometries; the grey area identifies the region of lower mass transfer compared to the steady state values; the results are plotted for $AR = 0.2;0.5;1$, $Wo = 7.9$

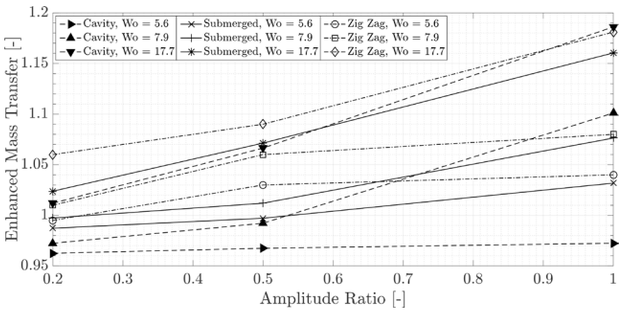

Fig. 15. Time and spatial integrated enhanced mass transfer for different amplitude ratios and Womersley numbers (lower membrane).

This explains why the literature review showed contradictory results. Here it can be seen that a wide range has to be investigated to gain an evidence about the mass transfer enhancement. Nevertheless, compared to the experiments found in literature, the enhanced mass transfer of pulsations in the simulations are much lower. It is assumed that there exist a lot of side effects like vibrations of the membrane, the damping characteristics due the elasticity of the membrane material and the amplitude form of the oscillations. Latter is difficult to compare between numerical and experimental results. As it is stated in [23], the numerical simulations are representing the right trends but the absolute values of mass or heat transfer enhancement differ significantly from the experiments, even in the laminar case.

5. Conclusion

In the present study dynamically operated reverse osmosis systems are numerically investigated using the OpenSource C++ library OpenFOAM by means of 2-D spacer filled channels. The implemented models are validated against literature data for typical brackish- and seawater desalination conditions. A discussion about the dynamics in the RO process showed that the mass transfer resistance of the membrane active layer is much lower than the mass transport resistance from the bulk to the membrane, which indicates that the dynamics of the active layer can be neglected. Nevertheless, the mass transfer resistance of the porous structure layer is higher and should be considered in future studies.

The performed simulations are 2-dimensional in space, to identify phenomena occurring in 3D spacer filled channels separately. Depending on flow attack angle and cross section, 3D spacer filled channels can be interpreted as a combination of the three considered geometries. Nevertheless, the results, especially the mass transfer enhancement studies can give the right trends with a smaller computational effort.

The analysis of the flow patterns show that the occurring phenomena disturbing the boundary layer differ significantly from the open-channel (Richardson effect, flow reversal). The concentration boundary layer in open channels in laminar flows is mainly influenced by diffusion due to the stratified flow patterns. In channels with turbulence promoters, the influence of the momentum normal to the membrane plays an important role and the mass transport problem changes from a diffusion dominated to a convection-diffusion problem inside the boundary layers. Additionally, this means that the influence of different frequencies and amplitudes differs completely in open and spacer filled channels and cannot be compared to each other. This could also explain the difference between literature data and simulated results.

The simulation results show that in pulsating flows in spacer filled channels, the concentration profiles near the attachment points of filament and membrane are only marginally influenced, because the momentum is significantly lower. A 3D simulation has therefore to be done, how this holds for the real spacer geometry. The main influence can be identified in the middle between two filaments.

At a very high Womersley number the flow structure and the mass transfer significantly differ from the steady state. A further study of the phenomena between these two frequencies has to be done. An analysis of the Sherwood number indicated that the mass transfer is more influenced by changing the Womersley number than by changing the amplitude ratio.

This study showed that a wide range of frequencies and amplitude ratios has to be investigated to identify the potential of pulsating flows for enhancement or decrease of mass transfer compared to steady state operation due to the complex flow phenomena. The gained results indicate that there can be a significant enhancement, depending on the chosen frequency and amplitude, but the frequencies have to be much higher than recommended in literature or occurring in RO systems transiently powered by renewable energies. It is therefore assumed that the performance enhancement due to a varying power supply by renewable energies will not be existent, but an active control can have a potential to significantly improve the RO process and possibly decrease the energy consumption.

Acknowledgements

The authors gratefully acknowledge financial support from the German Federal Ministry of Education and Research (BMBF) in the project PV/T-RO (02WA1299) within which this paper was developed. The responsibility for the content stays with the authors.

Symbols

Abbreviations

AR	–	Amplitude ratio
ECP	–	External concentration polarization
EMT	–	Enhanced mass transfer
GCI	–	Grid convergence index
RO	–	Reverse osmosis
SWM	–	Spiral wound modules

Domains and boundaries

Γ	–	Domain boundary
Γ_g	–	Dirichlet boundary
Γ_h	–	Neumann boundary
Ω	–	Fluid domain

Dimensionless numbers

Γ_{cp}	–	Concentration polarization factor
Bi	–	Biot number
Pe	–	Peclet number
Re	–	Reynolds number
Sh	–	Sherwood number
Wo	–	Womersley number

Scalars

β	Mass transfer coefficient	m/s
$\dot{m}$	Mass flow rate	kg/s
μ	Dynamic viscosity	Pa s
ν	Kinematic viscosity	m^2/s
ω	Angular frequency	Hz
ϕ	Mass fraction	–
π	Osmotic pressure	N/m^2
ρ_i	Mass concentration/density	kg/m^3
A	Area	m^2
A_m	Water permeability	$m^3/(m^2\ s\ bar)$
B_m	Salt permeability	$m^3/(m^2\ s)$
C_p	Heat capacity	J/(kg K)
D	Diameter	m
D_{AB}	Diffusion coefficient	m/s^2
e	Error	–
f	Frequency	Hz
J	Flux	$m^3/(m^2\ s)$
L	Length	m
L_0	Membrane thickness	m
p	Pressure	N/m^2
S	Structure parameter	m
T	Temperature	K
t	Time	s

Subscripts

Al	–	Active layer
bulk	–	Bulk
F	–	Feed
f	–	Fluid
mem	–	Membrane
P	–	Permeate
PS	–	Porous structure
W	–	Water
wall	–	Wall

Vectors and tensors

$\boldsymbol{\sigma}$	–	Cauchy stress tensor
$\boldsymbol{\varepsilon}$	–	Strain rate tensor
$\mathbf{u}'(\mathbf{x},t)$	–	Turbulent oscillating velocity vector
$\mathbf{b}$	–	Body force vector
$\mathbf{h}$	–	Neumann vector
$\mathbf{I}$	–	Identity vector
$\mathbf{n}$	–	Unity normal vector
$\mathbf{u}$	–	Velocity vector
$\mathbf{u}'$	–	Velocity fluctuation vector
$\mathbf{u}_0$	–	Mean velocity vector
$\tilde{\mathbf{u}}(\mathbf{x},t)$	–	Periodic velocity vector

References

[1] F. Zamani, J.W. Chew, E. Akhondi, W.B. Krantz, A.G. Fane, Unsteady-state shear strategies to enhance mass-transfer for the implementation of ultrapermeable membranes in reverse osmosis: A review, Desalination, 356(0) (2015) 328–348.

[2] A. Emad, A. Ajbar, I. Almutaz, Periodic control of a reverse osmosis desalination process. J. Process Control, 22(1) (2012) 218–227.

[3] A.P. Reverberi, V.P. Meshalkin, C. Cerrato, Yu. O. Savina, Dynamics of a reverse osmosis unit with application to pulsating regimes for process optimization. Theor. Found. Chem. Eng., 45 (2010) 190–197.

[4] T.J. Kennedy, R.L. Merson, B.J. McCoy, Improving permeation flux by pulsed reverse osmosis. Chem. Eng. Sci., 29(9) (1974) 1927–1931.

[5] S. Ilias, R. Govind, Potential applications of pulsed flow for minimizing concentration polarization in ultrafiltration, Sep. Sci. Technol., 25(13–15) (190) 1307–1324.

[6] V.I. Baikov, P.K. Znovets, Membrane processes of separation of solutions in a pulsating flow. J. Eng. Phys. Thermophys., 77(4) (2004) 802–807.

[7] K. Haddad, Özgür Ertunç, M. Mishra, A. Delgado, Pulsating laminar fully developed channel and pipe flows. Phys. Rev. E, 81 (2010) 016303-1–016303-13.

[8] R. Smith, Contaminant dispersion in oscillatory flows, J. Fluid Mech., 114 (1982) 379–398.

[9] P.C. Chatwin, On the longitudinal dispersion of passive contaminant in oscillatory flows in tubes, J. Fluid Mech., 71 (1975) 513–527.

[10] B.B. Gupta, P. Blanpain, M.Y. Jaffrin, Permeate flux enhancement by pressure and flow pulsations in microfiltration with mineral membranes. J. Membr. Sci., 70(2) (1992) 257–266.

[11] M.Y. Jaffrin, L.H. Ding, B.B. Gupta, Rationale of filtration enhancement in membrane plasmapheresis by pulsatile blood flow. Life support systems: J. European Soc. Art. Organs, 5(2) (1987) 267–271.

[12] C.D. Bertram, M.R. Hoogland, H. Li, R.A. Odell, A.G. Fane, Flux enhancement in crossflow microfiltration using a collapsible-tube pulsation generator. J. Membr. Sci., 84(3) (1993) 279–292.

[13] A. Abbas, N. Al-Bastaki. Flux enhancement of RO desalination processes, Desalination, 132 (2000) 21–27.

[14] M. Al haj Ali, A. Ajbar, E. Ali, K. Alhumaizi, Optimization-based periodic forcing of RO desalination process for improved performance, Desal. Water Treat., 51(37–39) (2013) 6961–6969.

[15] Nader M. Al-Bastaki, A. Abbas, Periodic operation of a reverse osmosis water desalination unit, Sep. Sci. Technol., 33(16) (1998) 2531–2540.

[16] B.S. Richards, D.P.S. Capao, A.I. Schäfer, Renewable energy powered membrane technology. 2. the effect of energy fluctuations on performance of a photovoltaic hybrid membrane system, Environ. Sci. Technol., 42(12) (2008) 4563–4569.

[17] L. Richards, B.S. Richards, Schäfer, I. Andrea, Renewable energy powered membrane technology: Salt and inorganic contaminant removal by nanofiltration/reverse osmosis, J. Membr. Sci., 369(1–2) (2011) 188–195.

[18] G.L. Park, A.I. Schäfer, B.S. Richards, Renewable energy-powered membrane technnolgy: Supercapacitors for buffering resoruce fluctuations in a wind-powered membrane system for brackish water desalination, Ren. Energy, 50 (2012) 126–135.

[19] B.S. Richards, G.L. Park, T. Pietzsch, A.I. Schäfer, Renewable energy powered membrane technology: Brackish water desalination system operated using real wind fluctuations and energy buffering, J. Membr. Sci., 468 (2014) 224–232.

[20] B.S. Richards, B.S. Park, G.L.T. Pietzsch, A. Schäfer, Renewable energy powered membrane technology: Safe operating window of a brackish water desalination system, J. Membr. Sci., 468 (2014) 400–409.

[21] A.M. Thomas, A. Jain, The effect of pulsatile flows on the transport across membranes: an analytical and experimental study, Sep. Sci. Technol., 42 (2007) 1931–1944.

[22] C. Rodrigues, M. Rodrigues, V. Semiao, V. Geraldes, Enhancement of mass transfer in spacer-filled channels under laminar regime by pulsatile flow, Chem. Eng. Sci., 123(0) (2015) 536–541.
[23] A. Cardenas, Influence of enhanced heat transfer in pulsating flow on the damping character-istics of resonator rings, Dissertation, Technische Universität München, 2014.
[24] G.A. Fimbres-Weihs, D.E. Wiley, Review of 3d cfd modeling of flow and mass transfer in narrow spacer-filled channels in membrane modules, Chem. Eng. Process, 49 (2010) 759–781.
[25] M. Özdinç Çarpinlio˘glu, E. Özahi, An updated portrait of transition to turbulence in laminar pipe flows with periodic time dependence (a correlation study), Flow, Turb. and Comb., 89(4) (2012) 691–711.
[26] R. Akhavan, R.D. Kamm, A.H. Shapiro, An investigation of transition to turbulence in bounded oscillatory stokes flows part 2, numerical simulations, J. Fluid Mech., 225 (1991) 423–444.
[27] King, V. Cameron, Time-resolved PIV and pressure measurements of oscillating and pulsating flow in a diffuser, (2008). All Graduate Theses and Dissertations. Paper 106.
[28] G.M. Geise, D.R. Paul, B.D. Freeman, Fundamental water and salt transport properties of polymeric materials, Prog. Polym. Sci., 39 (2014) 1–42.
[29] M.J. Lighthill, The response of laminar skin friction and heat transfer to fluctuations in the stream velocity, Proc. R. Soc. London, Ser. A. Math. Phys. Sci., 224 (1954) 1–23.
[30] H.B. Winzeler, G. Belfort, Enhanced performance for pressure-driven membrane processes: the argument for fluid instabilities, J. Membr. Sci., 80(1) (1993) 35–47.
[31] K.P. Lee, T.C. Arnot, D- Mattia, A review of reverse osmsosis membrane materials for desalination – Development ot date and future potential, J. Membr. Sci., 370 (2011) 1–22.
[32] A. Miquel, G. Schock, Mass transfer and pressure loss in spiral wound modules, Desalination, 64 (1987) 339–352.
[33] Y. Luo, E. Harder, R.S. Faibish, B. Roux, Computer simulations of water flux and salt permeability of the reverse osmosis ft-30 aromatic polyamide membrane, J. Membr. Sci., 384 (2011) 1–9.
[34] F. Helfer, C. Lemckert, Y.G. Anissimov, Osmotic power with pressure retarded osmosis: Theory, performance and trends: A review, J. Membr. Sci., 453 (2010) 337–358.
[35] Y.Y. Liang, G.A.F. Weihs, D.E. Wiley, Cfd modelling of electro-osmotic permeate flux enhancement in spacer-filled membrane channels, J. Membr. Sci., 507 (2016) 107–118.
[36] D. Sumner, Two circular cylinders in cross-flow: A review, J. Fluids Struct., 26(6) (2010) 849–899.
[37] J. Schwinge, D. Wiley, D.F. Fletcher, Simulation of unsteady flow and vortex shedding for narrow spacer-filled channels, Ind. Eng. Chem. Res., 42 (2003) 4962–4977.
[38] P.J. Roache, Quantification of uncertainty in computations fluid dynamics, Annu. Rev. Fluid. Mech., 29 (1997) 123–160.
[39] D.F. Fletcher, D.E. Wiley, A computational fluids dynamics study of buoyancy effects in reverse osmosis, J. Membr. Sci., 245 (2004) 175–181.
[40] M.H. Sharqawy, J.H. Lienhard, S.M. Zubair, Thermophysical properties of seawater: A review of existing correlations and data, Desal. Wat. Treat., 16 (2010) 354–380.
[41] W. Malalasekera, H.K. Versteeg, An introduction to computational fluid dynamics-the finite volume method-second editions, Pearson Verlag, 2007.
[42] A. Alexiadis, D.E. Wiley, A. Vishnoi, R.H.K. Lee, D.F. Fletcher, J. Bao, Cfd modeling of reverse osmosis membrane flow and validation with experimental results, Desalination, 217 (2007) 242–250.
[43] P. Xie, L.C. Murdoch, D.A. Ladner, Hydrodynamics of sinusoidal spacers for improved reverse osmosis performance, J. Membr. Sci., 453 (2014) 92–99.

Appendix

Table A1
Comparison of the performed CFD simulations in this study and experimental results of Alexiadis et al. [39]

Pressure [bar]	Average feed inlet velocity [m/s]	Flux experiment [lm^{-2} h^{-1}] [39]	Flux simulation [lm^{-2}) h^{-1}]	Relative error [%]
8.987	0.153	24.58	24.68	0.39
8.987	0.166	26.06	24.75	5.02
8.987	0.186	22.89	24.86	8.61
8.987	0.191	25.45	24.89	2.21
8.987	0.206	25.17	24.95	0.86
8.987	0.212	27.58	24.98	9.43
8.987	0.218	22.22	25.00	12.52
8.987	0.219	26.37	25.01	5.18
8.987	0.219	26.58	25.01	5.92
10.987	0.115	28.25	28.19	0.23
10.987	0.122	27.65	28.25	2.18
10.987	0.166	25.22	28.60	13.40
10.987	0.167	25.35	28.61	12.86
10.987	0.199	28.82	28.80	0.08
11.987	0.108	29.36	30.29	3.18
11.987	0.134	31.18	30.58	1.91
11.987	0.147	27.34	30.70	12.30
11.987	0.159	32.79	30.79	6.10
11.987	0.180	29.60	30.94	4.53
11.987	0.193	30.70	31.02	1.05
13.987	0.076	32.75	34.01	3.84
13.987	0.102	34.00	34.54	1.58
13.987	0.128	36.93	34.91	5.46
13.987	0.147	33.86	35.13	3.74
13.987	0.154	35.89	35.18	1.97
13.987	0.160	34.04	35.24	3.52

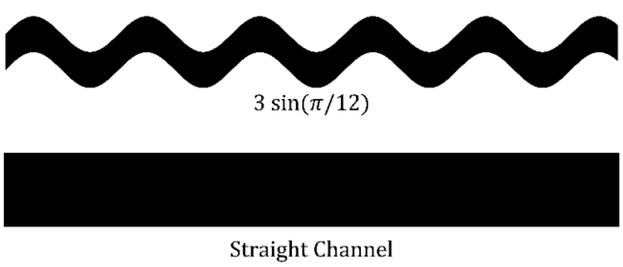

Fig. A1. Top view of the investigated membrane channels; adapted from [42].

Table A2
Comparison of time and local averaged mean Sherwood number of the transient CFD simulations

Spacer configuration	Womersley number	Amplitude ratio	Mean Sherwood number
Cavity (down)	0	0	37.49
Cavity (down)	5.6	1.0	35.25
Cavity (down)	7.9	0.2	35.57
Cavity (down)	7.9	0.5	36.02
Cavity (down)	7.9	1.0	38.85
Cavity (down)	17.7	1.0	57.44
Cavity (up)	0	0	45.93
Cavity (up)	5.6	1.0	43.60
Cavity (up)	7.9	0.2	42.33
Cavity (up)	7.9	0.5	43.26
Cavity (up)	7.9	1.0	46.18
Cavity (up)	17.7	1.0	65.96
Submerged	0	0	43.02
Submerged	5.6	1.0	45.86
Submerged	7.9	0.2	43.59
Submerged	7.9	0.5	45.47
Submerged	7.9	1.0	50.34
Submerged	17.7	1.0	62.45
Zig-zag	0	0	53.84
Zig-zag	5.6	1.0	58.51
Zig-zag	7.9	0.2	55.49
Zig-zag	7.9	0.5	59.53
Zig-zag	7.9	1.0	62.29
Zig-zag	17.7	1.0	90.09